

GMTNIRS – The High Resolution Near-IR Spectrograph for the Giant Magellan Telescope

D.T. Jaffe^{*a}, D.J. Mar^a, D. Warren^b, P.R. Segura^c

^aDept. of Astronomy C1400, Univ. of Texas at Austin, 1 University Station, Austin TX 78712

^bLos Angeles, CA

^cMcDonald Observatory C1402, Univ. of Texas at Austin, 1 University Station, Austin TX 78712

ABSTRACT

We present a conceptual design for a powerful, high-resolution near-infrared spectrograph for the Giant Magellan Telescope (GMT). This instrument, the Giant Magellan Telescope Near-Infrared Spectrograph (GMTNIRS), uses silicon immersion gratings as the primary dispersing elements. The design has two modules, one for 1.1-2.4 μm for use under native seeing conditions and one for 3-5.5 μm to be used with adaptive optics. The resulting design is physically compact and allows us to cover entire infrared atmospheric windows in a single exposure with resolving powers up to 100,000.

Keywords: silicon, immersion grating, GMT, spectrograph, high resolution, near-infrared

1. INSTRUMENT SPECIFICATIONS

Investigations with a high-resolution near-infrared spectrograph operating at 1-5 μm play an important role in two of the main science priorities for the GMT: unlocking the secrets of planet and star formation and understanding the evolution of stellar populations and chemical elements. This paper presents a conceptual design for such an instrument. The experiments derived from these science priorities led to a set of specifications for GMTNIRS.

- | | |
|--------------------------------|--|
| 1. Operating Wavelength Range: | 1.1-5.5 μm , (desired 0.8-5.5 μm) |
| 2. Resolving Power: | 2×10^4 - 1.5×10^5 |
| 3. Coverage: | All of H, K, L, or M in a single exposure |
| 4. Noise Limits: | source photon noise (1.1-2.4 μm), background (2.5-5.5 μm). |

The resolving power specification depends on goals at particular wavelengths. In general, the higher resolving power is required for molecular absorption line studies at $\lambda > 3 \mu\text{m}$.

1.1 Optical design

Given the different factors driving the design, it is clear from the outset that it is not possible to produce an instrument that is optimal across the entire proposed wavelength range. As a starting point for this study, we therefore have separate modules for the short and long wavelength bands.

At the shorter end of the 1.1-2.4 μm range, where Strehls tend to be lower, or at lower resolving powers where the slit will be fairly large, a module designed for native seeing should have significantly greater throughput than that of an adaptive optics (AO) spectrograph. A native seeing instrument will also be able to take advantage of atmospheric conditions that are not optimal for AO. At the longer wavelengths (2.2-5.5 μm) where background radiation can seriously compromise sensitivity even at high spectral resolution, it is desirable to use AO to reduce the warm solid angle seen by the system. Furthermore, AO can reliably produce high Strehl images at these wavelengths over a broad range of atmospheric conditions. In our conceptual design, we therefore assume that the long wavelength module is used with AO and a slit width of $2\lambda/D$ to capture most of the power in the diffraction spike.

*dtj@astro.as.utexas.edu

First light for GMT is projected for the later part of the 2010's. Technical capabilities in two critical areas for this instrument, IR detector arrays and Si immersion gratings, are progressing rapidly. We therefore produced this design using an extrapolation of existing capabilities in these two areas while making use of existing devices or techniques for all other aspects of the instrument.

1.2 Long wavelength (3-5.5 μm) module

The long wavelength module (LWM, 3-5.5 μm) has the less demanding optical design. We set the parameters for this module by specifying a slit width of $2\lambda/D$, requiring a resolving power of at least 100,000 at 4.6 μm , and a sampling of at least 3 pixels across the slit at 3.5 μm . Our optimal design uses an R2.68 (L band) or R3.0 (M band) immersion echelle with a 45 mm collimated beam. In addition, we wish to cover all of the L or M bands in a single exposure. Our investigation has shown that we can reach this coverage for the M band with the 2048 \times 2048 arrays already being developed for JWST and can almost reach it for the L band. For complete coverage of L, we require 2650 pixels in the dispersion direction.

Figure 1 shows an optical layout of the long wavelength module. The $f/8$ beam of the telescope enters the cryostat through an antireflection (AR) coated window (not shown, see Fig. 5) and comes to a focus just inside the dewar (Fig. 1 bottom, center). A fold mirror brings the beam to an off-axis paraboloid which collimates the light to produce an image of the pupil where we place a cold stop in the shape of the 7 mirror GMT primary (represented by a ring). A second paraboloid then reimages at $f/8$ to the entrance slit (not shown). At 3.5 μm , the $2\lambda/D$ slit projects to 60 mas on the sky. Reflective slit jaws will fold the unused portion of the field back to an IR acquisition and guide camera system within the dewar. A third paraboloid (lower left of Fig. 1) collimates the beam and forms a pupil just inside the entrance face of the immersion grating (center).

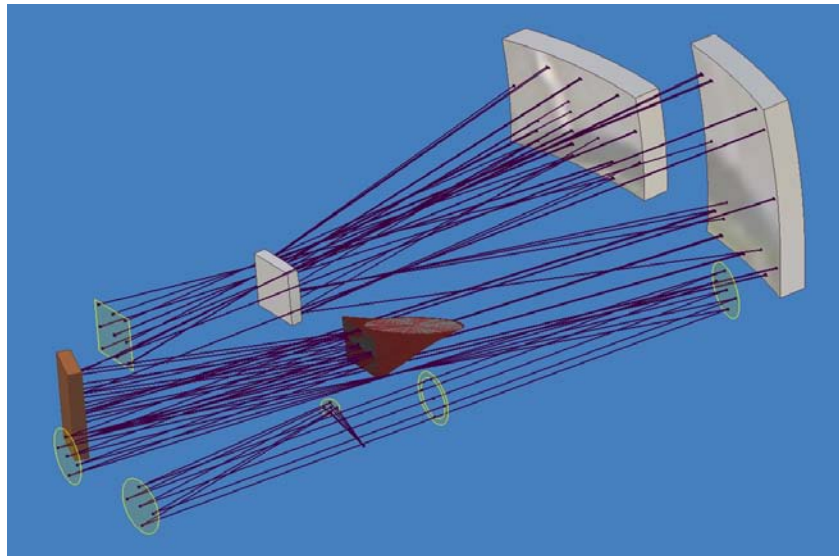


Figure 1. Solid surfaces for the pupil imager, grating/cross-disperser, and TMA/detector assemblies in the LWM.

A single immersion grating works well in producing continuous coverage of the L or M bands in a cross-dispersed spectrum. For our R2.68 grating, a groove width of 86 μm (the equivalent of 295 μm in vacuum) results in 3 pixel sampling at 3.5 μm and a resolving power $\lambda/\Delta\lambda$ of 117,000. At M band, with an R3 immersion grating with 160 μm groove spacing, the resolving power for a $2\lambda/D$ slit is 99,000. Even better resolving power could be achieved with a slightly larger array format and field of view, or with a larger immersion grating. In order to clear the beam entering the echelle from the collimator and the dispersed beam heading from the echelle to the cross-disperser, the echelle is tipped by 7° with respect to the beam from the collimator. The direction of this tip is perpendicular to the plane of the echelle dispersion. In immersion, at the grating itself, this cant is effectively smaller by a factor of the refractive index $n = 3.4$. To avoid a ghost reflection from the front surface of the echelle, the front and rear faces of the echelle are wedged with

respect to each other by a small angle. Most of any reflection from the front surface, however, is eliminated by a good AR coating.

Diffacted light reemerges from the front face of the immersion grating and goes directly to the cross disperser shown at the center left of Fig. 1. This element is a conventional front-surface grating. To achieve optimal formatting, we must use different immersion gratings and cross dispersers at L and M. Given the plate scale dictated by the sampling of the slit in the dispersion direction (20 mas per pixel), the order separation ranges from 0.6 arcsec to 1.27 arcsec across the L band for a 106 line/mm grating period using an incidence angle $\alpha = 2.4^\circ$, and the spectrum of the entire atmospheric window falls on the detector. For M band, a 113 line/mm cross disperser used at $\alpha = 8^\circ$ is optimal. The minimum order separation for this band is 0.85 arcsec.

After being dispersed and cross-dispersed, the beams from each wavelength are imaged onto the focal plane array (center left) by an all reflective three mirror anastigmat (TMA, upper right and center) with an effective focal length of 341 mm. The design is fairly simple with an ellipsoidal primary followed by a secondary and tertiary, both of which are spherical. Analysis of the sensitivity of the TMA's optical performance to misplacement and misalignment of its elements shows that the system is quite robust. Figure 2 shows spot diagrams for the beginning, middle, and end of the orders across the L band. Spots fall well within a single 18 μm pixel, implying that the optical performance is securely diffraction limited.

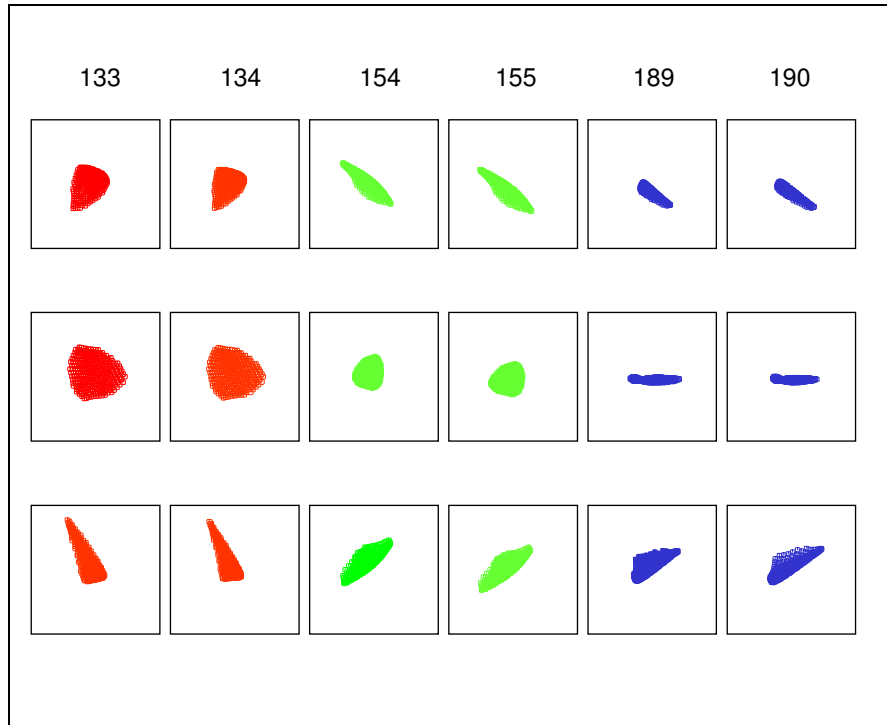


Figure 2. Geometric spot diagrams for L-band orders (each square is 18 μm \times 18 μm). Order numbers are indicated at the top.

1.3 Short wavelength (1.1-2.4 μm) module (SWM)

The short wavelength module will use the largest practical grating size. Extrapolating from the current state of the art in silicon immersion grating manufacture and from the current state of the semiconductor industry, this means a 300 mm long grooved surface. The highest resolution grating we can make at this size is an R3 immersion echelle with an 83 mm collimated beam. Given the refractive index of Si ($n \approx 3.4$ throughout the near-IR), this grating will have a diffraction limited resolving power, $R_{\text{diff}} = 1.72 \times 10^6 / [\lambda(\mu\text{m})]$. The diffraction-limited spatial resolution of the telescope is $\theta_{\text{diff}} = 8.4 \times \lambda$ milliarcsec. These parameters lead to resolving powers of 1×10^5 for a 0.15" slit and 2.5×10^4 for a 0.6" slit. Even at K band, the smallest slit is still significantly larger than the diffraction limit. These slit width-resolution

products are comparable to those available on high resolution IR spectrographs (CSHELL [Greene et al. 1993], PHOENIX [Hinkle et al. 1998], CRIRES [Käufl et al. 2004]) currently available on 4 and 8 m telescopes meaning that a comparable instrument will gain signal as the square of the aperture. Without the use of silicon immersion echelles, alternative designs for the SWM require collimated beam diameters that are larger (~285 mm) in order to achieve the same resolving power for a given slit width. The associated optical, optomechanical, and mechanical systems will be correspondingly larger, more complex, and more expensive.

To keep pixel sampling from being a limiting factor, we set the plate scale of the camera to put 2.25 pixels across the narrowest (0.15") slit. At the same time, we must produce a continuous spectrum of each of the infrared atmospheric windows: J, H, and K in a single exposure. The J window is shortened at the short wavelength end by absorption in the silicon immersion grating. To permit sky subtraction for point sources while always integrating on the target, we require at least 6 arcsec between spectral orders.

In the optical design, we assumed availability of a 4096 × 4096 array with a pixel pitch of 18 μm. The physical size of the pixels and the desired slit sampling sets the *f*-ratio of the camera at *f*/2.27. There will be anamorphic magnification in the spectrograph due to the echelle and cross-disperser being used off the Littrow condition. The cross-disperser typically produces the larger anamorphic contribution. We have optimized the format of the cross-dispersed spectrum for each atmospheric window separately. It turns out to be possible to get an appropriate format and good optical performance for J and H with a single immersion grating and two cross dispersers. A separate immersion grating and cross disperser are required for the K band. We discuss the format of the K band spectrum as an example of the design. Our K band immersion grating has a groove spacing of 25.1 μm. Placing 2.50 μm light in echelle order 66 gives continuous spectral coverage on the array, and covers the K band down to 2.05 μm in 15 orders. There are 3321/2.25 = 1476 resolved elements across each order. At the center of the K band, the width of order 72 is 0.023 nm, and the resolving power is 98,000. The groove width is equivalent to a width of 86 μm in vacuo, considerably coarser than any commercially available ruled gratings. A 354 line/mm conventional, front-surface cross-disperser used in-plane (no γ tilt) at an incidence angle $\alpha = 10.96^\circ$ disperses the echelle orders on the focal plane. The separation of the highest orders is 6.0 arcsec while the lowest orders are separated by almost 10 arcsec. There are 2189 pixels in the cross-dispersion direction.

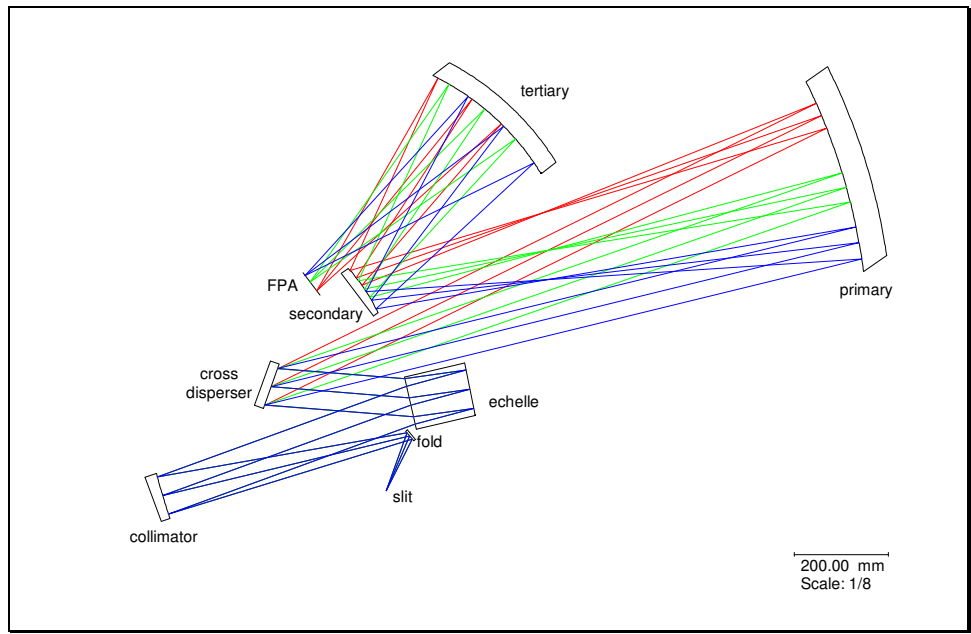


Figure 3. End-to-end optical model of the short wavelength module.

The optical layout of the SWM is similar to that shown in Fig. 1 for the LWM. The main difference between the two modules is the TMA camera. The effective focal length of the SWM TMA is only 188 mm and it must produce good images across an 18×16 degree field of view. Figure 3 is an optical layout of the SWM that demonstrates how the TMA camera dominates the scale of the instrument. All three TMA elements are off-axis aspheres with the primary being an ellipsoid and the secondary and tertiary oblate spheroids. Analysis of the optical design, however, indicates that all elements of the TMA are readily manufacturable and that displacement and alignment tolerances are not likely to cause significant difficulties in assembly.

We have performed a ray trace of the SWM in each spectral window. The results indicate that the system performs very well. In the K band, >98% of the energy falls within a single pixel, except at the extreme corners of the field where the energy on a single pixel is still 86% or greater. At almost all positions, virtually all rays fall within the $R=100,000$ slit.

1.4 Mechanical and cryogenic design

Because the SWM and LWM have different optimal cryostat temperatures and have different pickoff positions for the telescope beam in their respective wavelength ranges, our design places the two modules in separate cryostats. Both are modest in size for a high resolution IR instrument on a 20 m class telescope; the larger SWM cryostat has external dimensions of 2.25 m \times 1.5 m \times 1.0 m. The LWM cryostat is similar but only ~60% of this size. We discuss the mechanical design for both modules simultaneously, pointing out unique aspects as necessary.

Light from the telescope enters the modules through a warm box containing calibration lamps, an absorption cell, and flat-field sources. When observing an astronomical target, this box adds no surfaces to the optical path. The optomechanical design within the cryostat is greatly simplified for each module by the use of the same pupil reimager and collimator-camera optics in all wavelength bands and all configurations and by the ability of the instrument to observe an entire atmospheric window in a single exposure. The mechanical structure consists of four sections: (1) the pupil reimager, slit, and collimator, (2) the immersion echelle and cross-disperser, (3) the TMA and detector, and (4) the cryostat.

In the LWM, the pupil stop is permanently installed (see the bottom panel of Fig. 5). In the SWM, the pupil stop is removable to improve throughput at J and H where the background is negligible. Both modules will have a filter wheel containing broad-band blocking filters. The SWM has a wheel at the focal plane containing reflecting slit jaws, most likely with enough separate ports to allow the deckers to be part of each slit for each window. The slit wheel is the only element that is neither fixed nor moving between fixed end points. The wheel position will be encoded but will also be confirmable by observing the field with the slit viewing camera. This camera will permit rapid acquisition as well as near-simultaneous photometry of the targets. Current plans for the LWM call for a slide which will carry the two reflective slit plates.

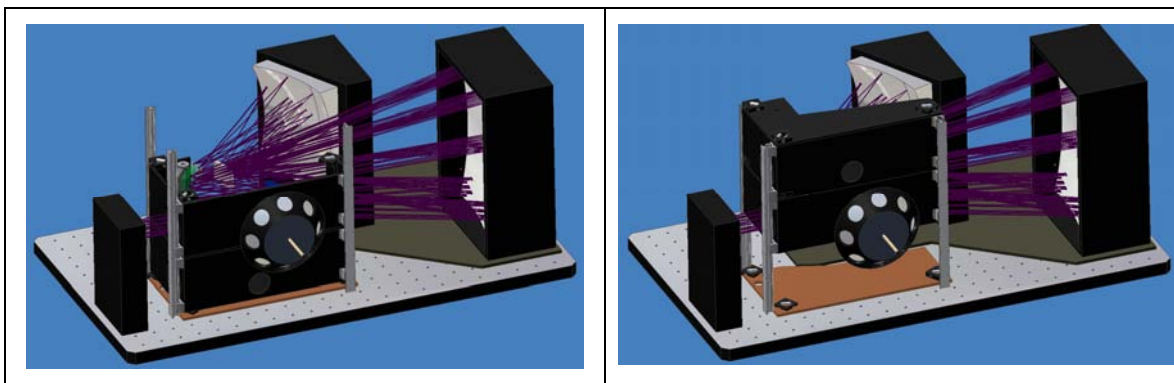


Figure 4. (left) SWM assembly of GMTNIRS with the grating/cross disperser assembly in the J/H-band configuration. The grating units are in their low position, and rest between the three vertical guide rails. One can see the J/H cross-disperser changer at the left. (right) The SWM in its K band configuration. The three hard stops on the optical bench are now visible below the unit.

Each module needs two immersion gratings. These are mounted into a unit containing their cross disperser or dispersers. The immersion grating is held in a fixed position within its unit and heat-strapped to the cold reservoir. For K, L, and M, the cross dispersers are also in fixed mounts. The J and H cross dispersers are mounted back to back and switch between two hard stops. Figure 4 illustrates how the two units in each spectrograph module can be exchanged. Above and below the units are hard-points which are mechanically secured to the optical bench. A drive mechanism pushes one of the units up against the upper or lower hard points to bring it into position.

The fabrication of the three TMA mirrors is potentially challenging, but well within the state-of-the-art of modern computer-controlled optical surfacing. The secondary and tertiary are small enough to be fabricated from their parent surfaces if this proves to be advantageous. The primary, because of its larger parent, would likely be generated directly as an off-axis section. Depending on the vendor and on the design details, the TMA will either be mounted as individual components, with alignment taking place from fiducial points using a Romer arm or other metrology tool, or it will be delivered from the manufacturer as a self-contained unit. All mounts will be CTE-matched to the mirror materials. The focal plane array will be thermally isolated from the 80 K optical bench and enclosed in a small housing. Both this housing and the chip carrier will be cooled to ~35 K via a heat strap tied to the second stage of the cryocooler.

In Figure 5, we show a cutaway view of the SWM cryostat. For the short wavelength module, the relatively low thermal background implies that to be source-limited the detector should operate below ~80 K and the optical system within the dewar can be somewhat warmer, around 120-140 K. For the best noise performance, the IR detector within the instrument should operate at the lowest temperatures consistent with the thermal power dissipation of the FPA and its support electronics. To meet these requirements, we baseline a cryostat for the short wavelength module in which the optics are at a temperature of 80 K and the FPA operates at ~35 K. For the long wavelength module, temperatures of less than ~60 K are required to keep the thermal radiation from the cryostat interior to negligible levels. The stability requirement of these temperatures will depend respectively on the thermal sensitivities of the optics, the optomechanical design, and the FPA performance.

In our design, the vacuum jacket is an aluminum box. Within this box is an aluminum radiation shield that is actively cooled and blocks radiation from the warm external wall of the cryostat. The shield is suspended by fiberglass G10 triangle structures. The shield will be covered in multiple layers of aluminized mylar superinsulation. Wrapping the shield in ~1 cm of superinsulation reduces the heat leak to 2 mW/cm². Assuming that the emissivities can be kept to 0.1 or below, we expect the heat load on the 80 K shield from radiation and subsequent "conduction" through the superinsulation to be ~28 W or less.

We have estimated the overall radiative and conductive loads and find that currently available cryocoolers can provide the necessary cooling capacity. The heat loads estimated above for the short wavelength module (55 W at 80 K, 5 W at 35 K) and the long wavelength module (40 W at 50 K, 4 W at 35 K) are consistent with experience drawn from other cryogenic near-IR spectrographs such as SpeX [Rayner et al. 2003] and PHOENIX [Hinkle et al. 2000]. In our conceptual design of the short wavelength module, the total cooling is achieved by connecting the first stage of a cryocooler to the cold shield and to the optical bench within it. This shield operates approximately at 80 K and sinks the external radiation and conductive loads. The interior surfaces of the shield are polished to reduce the emissivity, reducing the heat load on the FPA housing and any cold optical baffling structures that are attached to it. A second stage of a cryocooler is thermally anchored to the FPA housing, and operates at ~30 K. This stage maintains the temperature of the FPA at approximately 35 K by sinking the residual 80 K radiation from the cold shield and the heat generated by the FPA itself. Cooling connections to the 80 K stage should be duplicated for additional cooling power during cooldowns, and for redundancy.

We anticipate that the science FPA will take the form of a monolithic 4096 × 4096 HgCdTe array. Although no monolithic 4K × 4K format detector is available today, on the time scale of GMT it is virtually certain that such FPAs will be developed and become available. Several near-IR astronomical instruments on long (5-10 year) development times are aiming at the 4K × 4K format, and at least one vendor (Rockwell Scientific) has said that they are committing resources to development of these FPAs and associated support electronics. Prototypes of the Rockwell Scientific "HxRG" array could be available as early as later this year. Eventually, the array should be available in both short and long wavelength material (Table 1).

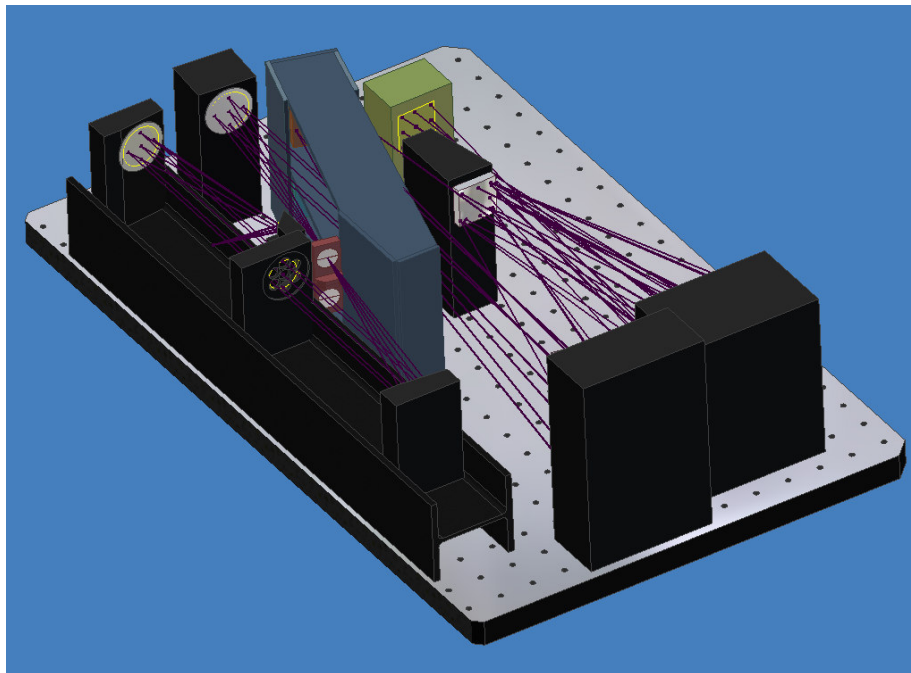
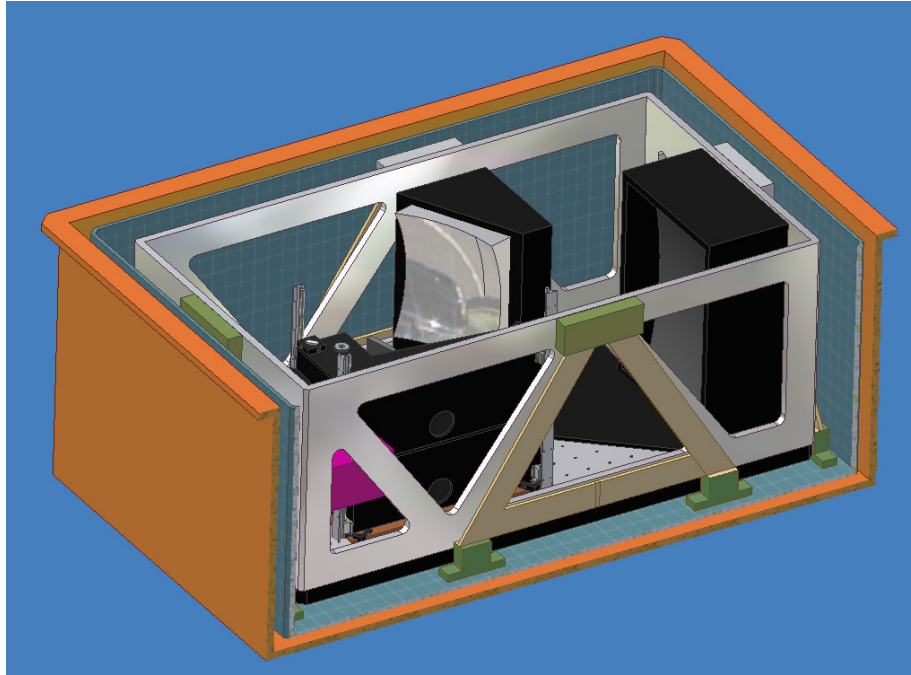


Figure 5 (top) Cutaway of the GMTNIRS short wavelength module cryostat (orange box). The beam enters the dewar from the missing side. Mylar superinsulation and the non-structural parts of the heat shields have been omitted for simplicity. The fiberglass triangles, of which one of four can be seen, connect the top of the 77K shield to the bottom of the dewar. A heat strap will connect the focal plane assembly and a small housing to the second stage of the cryocooler. (bottom) Optical assembly for the LWM, showing the pupil stop and the slits in the center of the figure (compare with Fig. 1).

Table 1. Specifications of the Rockwell-Scientific HAWAII 2-RG arrays, and preliminary performance data on Rockwell-Scientific's mosaic 4096 × 4096 prototypes. From the website of Rockwell-Scientific (2006), Ref. 7.

	2-RG, 2048 ²	4096 ² Mosaic prototypes
Readout rate	100 kHz to 5 MHz, continuously adjustable	
Spectral response	1.0 - 5.3 μm	0.3 - 6.0 μm, band-gap tunable
Operating temp.	~ 30 K	~ 30 K
Quantum efficiency	>65%	>80% with AR coating
Well depth	100000 e ⁻	>100000 e ⁻
Dark current (array mean)	~0.1 e ⁻ /s (2.5 μm @ 77 K)	0.02 e ⁻ /s (2.5 μm @78 K, 5 μm @37 K)
Fill factor	>98%	>98%
Read noise (array mean)	~15 e ⁻ /pixel (CDS, 100 kHz)	~15 e ⁻ /pixel (CDS, 100 kHz)
Integrated noise		6 e ⁻ rms (16/16, 100 kHz, 40 K, 1000 s)

The 4K × 4K HxRG FPA format is currently expected to have a pixel pitch of 15 μm (detector area is 61.44 mm × 61.44 mm), set mainly by the size of the detector substrate material. The smaller pixel size will necessitate minor adjustments to our optical design, which is based on the 18 μm pixel pitch of current arrays. The existing HAWAII-2RG focal plane arrays are designed to work with a companion application-specific integrated circuit (ASIC) called "SIDE CAR" [see Ref. 7] that can operate at 30-300 K. By placing the ASIC within the cryostat and close to the FPA, we will keep signal lines short and capacitances small. The ASIC dominates the cooling requirements, requiring more than twenty times the cooling power needed for the FPA. It is likely that the 4096 × 4096 array will be supported by a similar ASIC which GMTNIRS will use. The GMTNIRS software package will build on our experience with optical cross-dispersed spectrometers at McDonald Observatory [Tull et al. 1995, Tull 1998] and with the cryogenic mid-IR high-resolution spectrograph TEXES [Lacy et al. 2002], now a visitor instrument at Gemini North.

2. SILICON IMMERSION GRATINGS

Silicon immersion gratings, in which the infrared light is incident on a diffraction grating on the inside of a prism-shaped piece of crystalline silicon [Marsh, et al. 2006] offer significant advantages for high resolution infrared spectroscopy and are a critical enabling technology for GMTNIRS. Because the refractive index of silicon (3.44) results in a larger phase difference along the grating, a spectrograph using a silicon immersion grating will have an order of magnitude smaller collimated beam area than the beam area needed with a conventional front-surface grating for a given slit width-resolving power product. In addition, silicon micromachining techniques permit us to make very coarse gratings that enable cross-dispersed spectrograph designs with continuous rather than fragmented wavelength coverage. Without the use of immersion grating technology, it is unlikely that a near-IR spectrograph of comparable spectral performance to GMTNIRS could be designed to fit within the allowable space.

The University of Texas at Austin IR group has spent the past 15 years developing techniques to produce silicon immersion gratings [Moore et al. 1992, Graf et al. 1994]. Our approach has been to fabricate, test, model, and understand the gratings step by step and to publish detailed results [Jaffe et al. 1998, Ershov et al. 2001, Keller et al. 2000, 2002, Marsh et al. 2003]. We have produced several generations of silicon micromachined diffraction gratings leading up to the current generation of scientific-grade immersion gratings blazed for R2 [Marsh et al. 2006]).

High purity silicon is transparent at wavelengths from just above the short wavelength cutoff at ~1.1 μm at 77 K [MacFarlane et al. 1958] out to ~8 μm [Becker and Fan 1949], beyond the end of the M band. For the R3 echelles in the SWM, the round trip distance at the beam center is (90 mm) × (3/2) × 2 = 270 mm. Over the 1.1-5.5 μm operating band of GMTNIRS, the infrared absorption is expected to be largest at the short wavelength cutoff. Using a 8 mm thick double-sided polished FZ Si disk of high purity (resistivity > 1000 ohm-cm), the measured absorption coefficient at 77 K is $\alpha = 0.0133 \text{ cm}^{-1}$ at $\lambda = 1.10 \text{ μm}$, in good agreement with the data from MacFarlane et al. (1958) and the temperature dependence found for "high-purity" Si: $\alpha(T) = [T/(172.3 \text{ K})]^{4.25} \text{ [cm}^{-1}]$ at $\lambda = 1.064 \text{ μm}$ [Svantesson and Nilsson (1979)]. The corresponding absorption loss at 77 K in these echelles is expected to be $1 - \exp(-0.0133 \text{ cm}^{-1} \times 27 \text{ cm})$, or ~30% at $\lambda = 1.10 \text{ μm}$. At $\lambda = 1.15 \text{ μm}$, the absorption coefficient decreases slightly to $\alpha = 0.0085 \text{ cm}^{-1}$, and the absorption loss is

correspondingly smaller (~20%). For λ between 1.2 μm and 2.5 μm , the absorption is negligible. For the LWM, the round trip distance is half that of the short-wavelength module. We do not have reliable absorption data at 77 K for FZ Si in the L and M bands, but can extrapolate modest-resistivity Si data [Runyan 1965] to estimate the absorption coefficient for high purity FZ material to be $\alpha \sim 5 \times 10^{-4} \text{ cm}^{-1}$ at 77 K for $\lambda = 2\text{-}5 \mu\text{m}$. Absorption in the long wavelength echelles is therefore expected to be about 1% or less.

As specified by the optical design, the collimated beam diameters for the SWM ($\lambda = 1.1\text{-}2.5 \mu\text{m}$) and the LWM ($\lambda = 2.9\text{-}5.5 \mu\text{m}$) measure 83 mm and 45 mm respectively. For each of these modules we will need to fabricate two monolithic silicon immersion echelles with sufficiently large gratings to cover the elliptical projections of the beams. The largest echelles are for the SWM, requiring illuminated elliptical grating areas with minor axis = 83 mm and major axis = 249 mm (for R3, grating angle = 71.565°). This size requirement represents a scale-up of approximately a factor of 3 to 4 in each linear dimension from the largest complete grating (an R2 immersion echelle) currently in hand [Marsh et al. 2006]. To provide for mounting and alignment, the dimensions of the entrance face will be slightly larger, approximately 90 mm \times 90 mm. The echelle size requirements for the LWM are approximately half those for the SWM and the precision tolerances are less demanding. There are no significant technological barriers to fabrication of the larger gratings.

To minimize reflection losses at the entrance/exit face of each immersion echelle, a broadband antireflection (BBAR) coating will be applied to this surface. In GMTNIRS, each immersion grating will operate only over a single atmospheric window (except in the case of J and H), so the individual BBAR coatings can be optimized for fairly narrow wavelength ranges. To increase reflectivity, the groove facets are metallized by sputtering an aluminum film onto them [Marsh et al. 2006]. Figure 6 shows a scanning electron micrograph of aluminized silicon grooves.

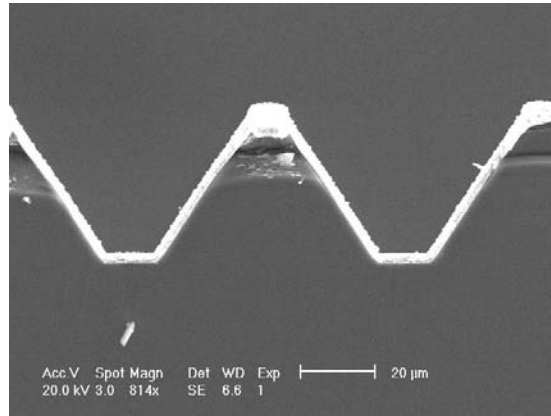


Figure 6. SEM micrograph of sputtered aluminum on a silicon witness piece into which a grating has been partially etched. The silicon is at the bottom of the figure. The aluminum layer appears bright in the micrograph. It is contiguous and completely covers the grating facets.

3. SENSITIVITY ESTIMATES

There are three relevant sensitivity regimes for high resolution spectroscopy in the near-infrared. At low (signal to noise) S/N, at higher resolving power, and at the shorter wavelengths, read noise dominates. When performing high S/N spectroscopy at short wavelengths, the photon shot noise of the source dominates. At longer wavelengths and lower resolving power, background noise becomes most important.

The number of background photons n_{bg} incident on a single pixel is given by $n_{bg} = (B_\nu/h\nu) \Delta\nu A\Omega m\epsilon$, where B_ν is the blackbody function at the ambient temperature, $\Delta\nu$ refers to the bandwidth transmitted by the slit, $A\Omega$ is the diffraction limited area-solid angle product and is equal to c^2/v^2 , m is the number of diffraction limited modes incident on a pixel, and ϵ is the combined emissivity of the atmosphere, telescope, and warm instrument surfaces, assuming that a cold stop has masked the unfilled portions of the telescope aperture. We therefore have $n_{bg} = 2\nu(e^{h\nu/kT} - 1)^{-1}(\epsilon m/R)$, where R is the slit-limited resolving power. For the SWM, each pixel has a width of 0.0667 arcsec while, for the LWM, the pixel width is 0.02 arcsec. With these scales, we have $m = 52.3/\lambda^2$ and $m = 4.7/\lambda^2$, respectively, for the SWM and LWM. The number of noise electrons in a given exposure time t , taking into account all noise sources, is then given by $n_{noise}^2 =$

$n_{\text{read}}^2 n_{\text{pix}} + (n_{\text{source}} + n_{\text{bg}} n_{\text{pix}}) \eta t$, where n_{pix} is the number of pixels included in the average (usually the number of pixels corresponding to the slit width times the full width to half maximum of the image) and η is the optical throughput of the atmosphere, telescope, and instrument times the QE of the detector. The number of source photons contributing to the signal is $n_{\text{source}} = N_{\text{zm}}(\nu) (\nu/R) 10^{-0.4 m(\nu)} \eta t$, where $N_{\text{zm}}(\nu)$ is the number of photons per unit frequency incident on the telescope from a zero magnitude star and $m(\nu)$ is the source magnitude at the same frequency.

Table 2. Limiting magnitudes for point sources. The table assumes two 30 minute integrations with the source on the slit in both exposures.

band	λ (μm)	R	Limiting Magnitude	
			S/N=10	S/N=100
J	1.22	50,000	19.6	16.0
H	1.65	50,000	19.1	15.5
K	2.16	50,000	18.1	14.1
L	3.55	133,000	14.5	11.9
M	4.77	100,000	12.1	9.6

Given a set of reasonable assumptions about seeing, telescope and instrument throughput, and detector performance, we have used this formalism to make a preliminary estimate the limiting magnitudes for observations of point sources at S/N = 10 and S/N = 100. These numbers are calculated assuming two half-hour integrations. In the background and source noise limits, the exposures can be broken into smaller units with no loss of sensitivity. For J, H, and K, we calculate the limiting magnitudes for $R = 50,000$. For L and M, where AO is used, we calculate the limiting magnitudes for $R = 133,000$ and $100,000$, respectively. The limiting magnitudes are listed in Table 2. In all cases, the S/N is for a single resolution element. Performance will be poorer off the blaze and at higher airmass.

4. CONCLUSION

GMTNIRS will provide a powerful new tool for studies of star and planet formation and for investigations of the chemical evolution of the Galaxy. There are currently two instruments on 8 meter class telescopes that cover the same wavelength range at comparable resolving power. These are PHOENIX [Hinkle et al. 2000], currently at Gemini South, and CRIRES [Wiedemann et al. 2000] at the VLT. Both of these are single-order instruments with maximum resolving powers in the range of 70,000 for slit sizes of 0.15-0.2". CRIRES has the larger instantaneous wavelength coverage but this only amounts to $\lambda/70$. Based on its significantly larger instantaneous coverage (20 times that of CRIRES) and on the preliminary sensitivity estimate, GMTNIRS will realize very substantial gains over current high resolution spectrographs in the near-IR.

REFERENCES

1. Greene, T.P., Tokunaga, A.T., Toomey, D.W., and Carr, J.S., 1993, Proc. SPIE 1946, 313
2. Hinkle, K.H., Cuberly, R., Gaughan, N., Heynssens, J., Joyce, R., Ridgway, S., Schmitt, P., and Simmons, J.E., 1998, Proc. SPIE 3354, 810.
3. Käufel, H.U., Ballester, P., Biereichel, P., Delabre, B., Donaldson, R., Dorn, R., Fedrigo, E., Finger, G., Fischer, G., Franza, F., Gojak, D., Huster, G., Jung, Y., Lizon, J.L., Mehrgan, L., Meyer, M., Moorwood, A., Pirard, J.F., Paufigue, J., Pozna, E., Siebenmorgen, R., Silber, A., Stegmeier, J., and Wegerer, S., 2004, Proc. SPIE, 5492, 1218
4. Richardson, R.C., and Smith, E.N., 1988, *Experimental Techniques in Condensed Matter Physics at Low Temperatures*, Addison-Wesley
5. Rayner, J.T., Toomey, D.W., Onaka, P.M., Denault, A.J., Stahlberger, W.E., Vacca, W.D., Cushing, M.C., and Wang, S., 2003, PASP 115, 362
6. Hinkle, K.H., Joyce, R.R., Sharp, N., and Valenti, J.A., 2000, Proc. SPIE 4008, 720
7. Rockwell-Scientific Company, 2006, http://www.rockwellscientific.com/imaging/standard_products.html
8. Tull, R.G., MacQueen, P.J., Sneden, C., & Lambert, D.L., 1995, PASP 107, 251
9. Tull, R.G., 1998, Proc. SPIE 3355, 387
10. Lacy, J.H., Richter, M. J., Greathouse, T.K., Jaffe, D.T., and Zhu, Q., 2002, PASP 114, 153

11. Marsh, J.P., Mar, D.J., and Jaffe, D.T., 2006, Proc SPIE, this volume
12. Moore, J., Ling, H., Graf, U.U., and Jaffe, D.T., 1992, Microwave and Opt. Tech. Letters, 5, 480
13. Graf, U.U., Jaffe, D.T., Kim, E.J., Lacy, J.H., Ling, H., Moore, J.T., and Rebeiz, G., 1994, Appl. Opt. 33, 96
14. Jaffe, D.T., Keller, L.D., and Ershov, O.A., 1998, Proc. SPIE, 3354, 201
15. Ershov, O.A., Jaffe, D.T., Marsh, J.P., and Keller, L.D., 2001, Proc. SPIE, 4440, 301
16. Keller, L.D., Jaffe, D.T., Ershov, O.A., Benedict, T., and Graf, U.U., 2000, Appl. Opt., 39, 1094
17. Keller, L.D., Jaffe, D.T., Ershov, O.A., and Marsh, J.P., 2002, Proc SPIE, 4485, 385
18. Marsh, J.P., Ershov, O.A., and Jaffe, D.T., 2003, Proc. SPIE, 4850, 797
19. MacFarlane, G.G., McLean, T. P., Quarrington, J. E., and Roberts, V., 1958, Phys. Rev. 111, 1245-1254
20. Becker, M. and H.Y. Fan, 1949, Phys. Rev. 76, 1531
21. Svantesson, K.G., and Nilsson, N.G., 1979, J. Phys. C 12, 3837
22. Runyan, W.R., 1965, *Silicon Semiconductor Technology*, McGraw-Hill
23. Wiedemann, G., Delabre, B., Huster, G., Moorwood, A., and Sokar, B., 2000, Proc. SPIE 4008, 1076